nature communications

Article

https://doi.org/10.1038/s41467-025-64537-1

Enhancing radiostrontium uptake by a layered titanate perovskite via sustainable electrochemically switched ion exchange

Received: 19 May 2025

Accepted: 17 September 2025

Published online: 27 October 2025

Check for updates

Zhi-Hua Chen[1,2], Feng-Hua Ding[3], Shao-Qing Jia[4], Hai-Yan Sun[1], Shuang-Jiang Li[1], Jun-Hao Tang[1], Xiao-Ying Huang[1,2], Mei-Ling Feng[1,2,5] ✉ & Zhang Lin[1,3] ✉

Green and sustainable ^{90}Sr uptake is urgently needed for radionuclides remediation. Herein, we propose an efficient strategy based on electrochemically switched ion exchange (ESIX) method to enhance ^{90}Sr uptake using electroactive ion exchange material. A titanate perovskite ($Na_2La_2Ti_3O_{10}$) with outstanding acid, irradiation resistance, and thermal stability can effectively capture Sr^{2+} and achieve remediation of actual acidic ^{90}Sr-containing liquid waste ($R^{Sr} > 99\%$). $Na_2La_2Ti_3O_{10}$ is prepared as working electrode C@NaLaTiO to enhance Sr^{2+} uptake via ESIX. Remarkably, the Sr^{2+} adsorption capacity increases (from 104.84 to 175.43 $mg{\cdot}g^{-1}$) and high selectivity for Sr^{2+} is maintained even under strongly acidic solutions. The Sr^{2+} adsorption-desorption can be controlled via facile potential modulation. Mechanism study indicates that efficient Sr^{2+} capture originates from the ion exchange between Sr^{2+} and interlayer Na^+ in $Na_2La_2Ti_3O_{10}$ coupled with the electrochemical redox reaction between Ti^{4+}/Ti^{3+} and the increase in oxygen vacancy. Density functional theory calculations support that ESIX enhances Sr^{2+} adsorption by increasing the binding energy of anionic $[La_2Ti_3O_{10}]_n^{2n-}$ layers towards Sr^{2+}. This study offers a convenient and environmentally friendly way for the efficient ^{90}Sr enrichment from radioactive waste liquids.

The sustainable development of the nuclear industry is closely linked to properly disposing of radioactive waste. As one of the most dangerous radionuclides in the ^{235}U fission products, ^{90}Sr ($t_{1/2}$ ~ 28 years) exists in the form of ions ($^{90}Sr^{2+}$) in radioactive liquid waste and releases β rays[1–3]. Due to its chemical similarity to calcium, $^{90}Sr^{2+}$ can accumulate in bones once entering the human body, which may lead to serious health problems (such as bone cancer and leukemia)[4,5]. Furthermore, the high solubility and easy environmental mobility make $^{90}Sr^{2+}$ a significant threat to ecosystems[1,4]. For instance, after the Fukushima nuclear accident in 2011, the concentration of ^{90}Sr was found to be four orders of magnitude higher than the environmental background level in the offshore waters, which aroused people's concern about the safety of nuclear energy[6]. Therefore, the development of green and efficient methods to remove ^{90}Sr from radioactive liquid waste is of great significance for environmental protection and human health.

Ion exchange method has been widely employed for the removal of Sr^{2+} from radioactive liquid waste[2]. However, traditional ion exchange materials such as resins, clays, and zeolites suffer from low adsorption capacity and poor selectivity for Sr^{2+}, especially in acidic or high-salinity environments due to their poor chemical stability and interference from competitive ions[7]. The electrochemically switched ion exchange (ESIX) method has emerged as a promising approach for the efficient removal of radionuclides, which synergistically combines

[1]State Key Laboratory of Structural Chemistry, Fujian Institute of Research on the Structure of Matter, Chinese Academy of Sciences, Fuzhou, PR China. [2]University of Chinese Academy of Sciences, Beijing, PR China. [3]School of Metallurgy and Environment, Central South University, Changsha, PR China. [4]HTA Co. Ltd., Beijing, PR China. [5]Fujian Province Joint Innovation Key Laboratory of Fuel and Materials in Clean Nuclear Energy System, Fujian Institute of Research on the Structure of Matter, Chinese Academy of Sciences, Fuzhou, PR China. ✉e-mail: fml@fjirsm.ac.cn; zhang_lin@csu.edu.cn

electrochemical adsorption with ion exchange[8]. This technique employs controlled electrical potentials to modulate redox states in electrode materials accompanied by the occurrence of ion exchange, enabling dynamic control over ion capture and release processes. Compared with the traditional ion exchange method, ESIX can significantly enhance the adsorption capacity by adjusting the voltage and minimize the formation of secondary pollutants in a more sustainable and environmentally friendly way[9,10]. The key of ESIX is to develop electrode materials with excellent structural stability that can dynamically respond to electric fields and meanwhile possess ion exchange properties. To date, hexacyanoferrates have been explored for ESIX applications due to their ion exchange performance and reversible redox reaction between Fe^{3+} and Fe^{2+}, particularly for the removal of Cs^+ ions[11]. For instance, nickel hexacyanoferrate/porous three-dimensional carbon felt (NiHCF/PTCF) and iron hexacyanoferrate/graphene/carbon fibers composite (PB/GN/CFs) have both demonstrated significant Cs^+ uptake capacity through ESIX[12,13]. Other inorganic materials containing metals with variable valency have been used for Cs^+ removal through ESIX, for example, Mo(VI)-based inorganic material $Na_{1.5}Mo_6O_{18}$[14]. However, ESIX has not yet been used to treat Sr^{2+}, which may originate from the fact that the large hydration radii and high valency of Sr^{2+} can lead to difficulty in ion mobility and reversible insertion[15].

Perovskite-type oxides have emerged as a versatile class of materials with excellent water stability, tunable structures, and abundant active sites, making them ideal for applications in radionuclides adsorption[16–20]. Three-dimensional (3D) perovskite-type oxides such as $CaAlO_x$, $CaTiO_x$, and $CaTiO_3$ have shown high adsorption capacities for U(VI) due to their large specific surface areas and accessible adsorption sites[21,22]. On the other hand, two-dimensional (2D) perovskite-type oxides offer superior tunability in composition and structure, which render them promising in radionuclides adsorption[23]. 2D perovskite-type oxides are categorized into three main types: R-P-type (Ruddlesden–Popper, $A'_2A_{n-1}B_nO_{3n+1}$), D-J-type (Dion–Jacobson, $A'A_{n-1}B_nO_{3n+1}$), and AV-type (Aurivillius, $(Bi_2O_2)A_{n-1}B_nO_{3n+1}$)[24]. Among them, only D-J-type perovskite-type oxides ($HCa_2Nb_3O_{10}{\cdot}1.5H_2O$ and $HLaNb_2O_7$) have been reported for Cs^+ removal[25,26]. By contrast, the R-P-type perovskite-type oxides with two interlayer cations per formula unit possess twice the anionic charge density of the perovskite-type oxides. Therefore, R-P-type perovskite-type oxides possess anionic layers with a higher negative charge, which will be beneficial to have higher ion exchange capacities[27]. To date, however, R-P-type perovskite-type oxides remain underexplored for radionuclide capture.

R-P-type titanate perovskites, including $A_2La_2Ti_3O_{10}$ (A = Li, Na, K, Rb, and H) and $ALaTiO_4$ (A = Li, Na, K, and H), have been reported[28–30]. The presence of interlayer cations in their structures provides abundant exchangeable sites for adsorption. In addition, titanium can show a variety of valency states, including Ti^{2+}, Ti^{3+}, and Ti^{4+}, which endows layered titanates with good redox activity. As a result, titanates have been well-suited for electrochemically controlled adsorption and desorption processes[31,32]. For example, under the applied electric field, the Cs^+ adsorption capacity of $Na_2Ti_3O_7$ nanotubes is greatly enhanced due to the valency change of Ti[31]. The redox-active nature of R-P-type titanate perovskites, combined with their tunable structures and high stability, offers great potential for selective radionuclide removal via ESIX. Therefore, it is anticipated that incorporating electroactive R-P-type titanate perovskites into the ESIX system should be a promising strategy for improving the capture of radioactive Sr^{2+}.

Guided by this strategy, the R-P-type titanate perovskite $Na_2La_2Ti(IV)_3O_{10}$ with high acid, thermal, and irradiation stability is screened out. It exhibits high adsorption capacity (104.84 $mg{\cdot}g^{-1}$) and fast kinetics (30 min) for Sr^{2+} adsorption. $Na_2La_2Ti_3O_{10}$ demonstrates excellent treatment capability for actual acidic ^{90}Sr-liquid-waste generated during industrial production. When $Na_2La_2Ti_3O_{10}$ is prepared as the working electrode C@NaLaTiO for Sr^{2+} capture, under ESIX, the Sr^{2+} adsorption capacity increases significantly to 175.43 $mg{\cdot}g^{-1}$. Impressively, the selectivity for Sr^{2+} in highly acidic conditions (pH = 1) is improved by nearly two orders of magnitude (56.30 $mL{\cdot}g^{-1}$ to 2.23×10^3 $mL{\cdot}g^{-1}$). The Sr^{2+} adsorption mechanism is revealed and the efficient Sr^{2+} capture is attributed to the ion exchange between Sr^{2+} and interlayered Na^+ in $Na_2La_2Ti_3O_{10}$ and electrochemical adsorption. By employing an external potential field, Ti^{4+} is reduced to Ti^{3+}, causing the increase in oxygen vacancy and promoting Sr^{2+} adsorption in the interlayer space[33]. On the contrary, when Ti^{3+} is oxidized to Ti^{4+} under a reverse electric field, the material can achieve the desorption of Sr^{2+}. DFT calculations show that introducing ESIX enhances the binding energy of the anionic $[La_2Ti_3O_{10}]_n^{2n-}$ layers for Sr^{2+}, indicating enhanced interaction between the anionic layer $[La_2Ti_3O_{10}]_n^{2n-}$ and Sr^{2+} ions under applied voltage. This work not only advances the development of the ESIX system for Sr^{2+} uptake but also provides a sustainable approach for managing radioactive strontium contamination.

Results

Characterizations

The structure of $Na_2La_2Ti_3O_{10}$ features the anionic triple perovskite slabs of $[La_2Ti_3O_{10}]_n^{2n-}$ with interlayer Na^+ ions (Supplementary Fig. 1a)[34]. The triple perovskite slabs of $[La_2Ti_3O_{10}]_n^{2n-}$ are built up of $[TiO_6]$ octahedra in corner-sharing mode, while La^{3+} ions are cavitied in the intralyer spaces. The adjacent slabs are stacked with a displacement of 0.5 along the a-axis[24]. High-valency Ti^{4+} in the structure provides the redox condition for the treatment of Sr^{2+} by ESIX.

The Sr^{2+} adsorption product of $Na_2La_2Ti_3O_{10}$ is denoted as $Na_2La_2Ti_3O_{10}$-Sr. Energy dispersive spectroscopy (EDS) analysis and elemental distribution mapping confirm the successful adsorption of Sr^{2+} and its uniform distribution in the $Na_2La_2Ti_3O_{10}$-Sr sample (Supplementary Fig. 1b–d). The optical adsorption edges of $Na_2La_2Ti_3O_{10}$ and $Na_2La_2Ti_3O_{10}$-Sr are 3.21 eV and 3.34 eV, respectively (Supplementary Fig. 2a, b). By comparing the powder X-ray diffraction (PXRD) patterns of $Na_2La_2Ti_3O_{10}$-Sr with the simulated one of $Na_2La_2Ti_3O_{10}$, it can be found that the layered structure of $Na_2La_2Ti_3O_{10}$ is maintained before and after the adsorption of Sr^{2+} (Supplementary Fig. 2c, d). Thermogravimetric analysis (TGA) results show that there is almost no weight loss of $Na_2La_2Ti_3O_{10}$ from 25 to 1200 °C (Supplementary Fig. 2e). Due to the loss of adsorbed water molecules, $Na_2La_2Ti_3O_{10}$-Sr has a weight loss of 0.70% from 25 to 160 °C (Supplementary Fig. 2e). PXRD analyses confirm that $Na_2La_2Ti_3O_{10}$-Sr can maintain the original skeleton without collapsing after heating to 1200 °C. These results indicate excellent thermal stability of the current titanate perovskite (Supplementary Fig. 2f). Furthermore, by comparing the scanning electron microscope (SEM) images of $Na_2La_2Ti_3O_{10}$ and $Na_2La_2Ti_3O_{10}$-Sr, it is evident that $Na_2La_2Ti_3O_{10}$ exhibits a sheet-like morphology, whereas $Na_2La_2Ti_3O_{10}$-Sr maintains a similar sheet-like structure, albeit with a slight tendency toward pulverization (Supplementary Fig. 3a, b).

To confirm the acid stability of $Na_2La_2Ti_3O_{10}$, $Na_2La_2Ti_3O_{10}$ samples were placed in various solutions (pH = 7 to 4 $mol{\cdot}L^{-1}$ HNO_3) at room temperature (RT) with soaking for 12 h, respectively. In the pH range of 4 to 7, the PXRD patterns of the immersed materials are consistent with that of the original $Na_2La_2Ti_3O_{10}$ (Supplementary Fig. 3c). As the acidity increases from pH of 3 to 2 $mol{\cdot}L^{-1}$ HNO_3, the immersed samples transform into the $H_2La_2Ti_3O_{10}$ according to the PXRD results, whereas the layered framework remains stable (Supplementary Fig. 3c). More importantly, the leaching rates of La^{3+} and Ti^{4+} for $Na_2La_2Ti_3O_{10}$ in the pH range from 1 to 7 and even in 1–2 $mol{\cdot}L^{-1}$ HNO_3 solutions are less than 6.17% and 5.51%, respectively (Supplementary Fig. 3d and Table 1).

Further, $Na_2La_2Ti_3O_{10}$ was combined with carbon black and polyvinylidene fluoride, and then coated on the surface of carbon cloth to prepare the working electrode C@NaLaTiO for Sr^{2+} capture (Fig. 1a and Supplementary Fig. 4a, b). The adsorption product of C@NaLaTiO

https://doi.org/10.1038/s41467-025-64537-1

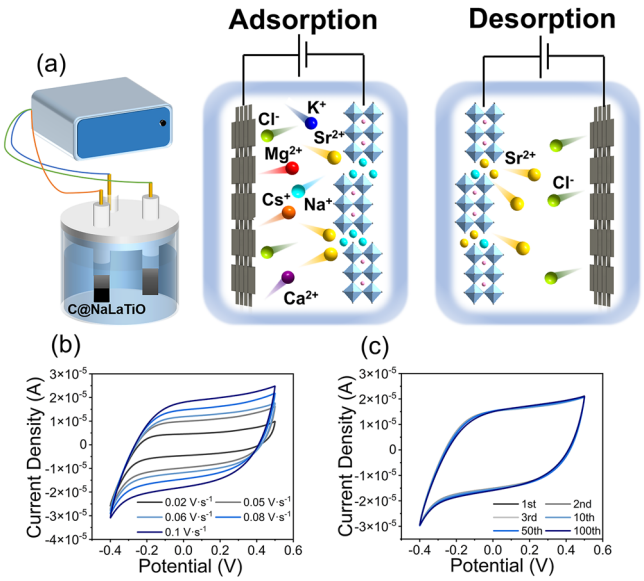

Fig. 1 | Schematic diagram of ESIX and the characterization of C@NaLaTiO. **a** Diagram of electrochemical adsorption and desorption process of Sr^{2+} on the C@NaLaTiO electrode. **b** CV curves of C@NaLaTiO at different scan rates in 50 mg·L^{-1} $SrCl_2·6H_2O$ solutions. **c** CV curves of C@NaLaTiO from the 1st to 100th cycle at 0.08 V·s^{-1} in 50 mg·L^{-1} $SrCl_2·6H_2O$ solutions. Source data are provided as a Source Data file.

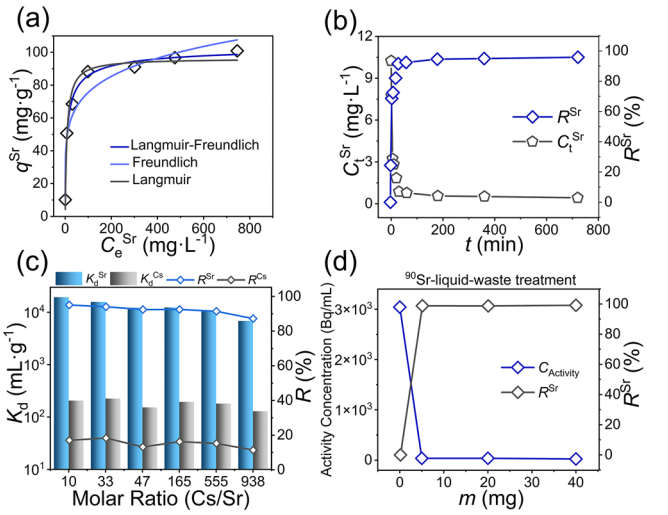

Fig. 2 | The Sr^{2+} removal performance of $Na_2La_2Ti_3O_{10}$. **a** The Sr^{2+} adsorption equilibrium data of $Na_2La_2Ti_3O_{10}$ fitted with the Langmuir, Freundlich, and Langmuir-Freundlich isotherm models. **b** The kinetics curve of $Na_2La_2Ti_3O_{10}$ for Sr^{2+} adsorption. **c** K_d (mL·g^{-1}) and R (%) of $Na_2La_2Ti_3O_{10}$ for Sr^{2+} and Cs^+ removal under different Cs/Sr molar ratios. **d** The treatment capacity of $Na_2La_2Ti_3O_{10}$ for 5 mL acidic (pH = 3.75) ^{90}Sr-liquid-waste plotted as radioactivity concentration and R^{Sr} (%) *vs* the mass of adsorbent (mg), respectively. Source data are provided as a Source Data file.

is denoted as C@NaLaTiO-Sr. EDS analysis confirms the successful Sr^{2+} adsorption and uniform distribution in C@NaLaTiO-Sr (Supplementary Fig. 4c, d). Cyclic voltammograms of C@NaLaTiO in the solutions (50 mg·L^{-1} $SrCl_2·6H_2O$) at different scanning rates of 0.02–0.1 V·s^{-1} were tested (Fig. 1b). It can be seen that the redox peak is very wide, indicating that C@NaLaTiO has good electrochemical activity. As the scanning rate increases, there is a peak shift, but the overall shape of the redox peak remains, which means that the capacity of C@NaLaTiO is still reversible even at high scanning rates. The diffusion-controlled contribution reaches 66.83% at 0.08 V·s^{-1}, suggesting that the partial current generated by the insertion and release of Sr^{2+} in the interlayer space has a significant effect on the total current (Supplementary Table 2). In addition, when the scanning rate increases from 0.02 V·s^{-1} to 0.1 V·s^{-1}, the capacitance contributions increase from 50.29% to 69.23%. Therefore, the kinetics of the capacitance contribution on the surface is a rate-determining process rather than a diffusion-controlled process[9]. Furthermore, after 100 times of the electrochemical redox process, the CV curves do not change significantly, which proves that C@NaLaTiO has good stability during the electrochemical process (Fig. 1c). Additionally, there is no obvious change in the CV curves after 100 electrochemical redox processes in the voltage range of −4 V to 4 V, demonstrating the exceptional cycling stability of C@NaLaTiO under high-voltage operation (Supplementary Fig. 4e). The SEM images of C@NaLaTiO and C@NaLaTiO-Sr reveal a characteristic stacked plate-like morphology, which facilitates efficient ion transport pathways and provides abundantly accessible sites for Sr^{2+} adsorption (Supplementary Fig. 4f, g).

Batch adsorption experiments of $Na_2La_2Ti_3O_{10}$

The adsorption capacity of $Na_2La_2Ti_3O_{10}$ for Sr^{2+} at RT has been measured by static batch adsorption experiments. The Sr^{2+} adsorption equilibrium curve of $Na_2La_2Ti_3O_{10}$ has been fitted with the Langmuir, Freundlich, and Langmuir-Freundlich adsorption isotherm models (Fig. 2a and Supplementary Table 3)[35]. It is found that the isotherm curve can be better fitted with the Langmuir-Freundlich isotherm model with a higher correlation coefficient of 0.99028 (Supplementary Table 4). According to the Langmuir-Freundlich adsorption isotherm model, the maximum Sr^{2+} adsorption capacity (q_m^{Sr}) of $Na_2La_2Ti_3O_{10}$ is 104.84 mg·g^{-1} (Supplementary Table 4). Compared with $Na_2Ti_nO_{2n+1}$ (49.6 mg·g^{-1}), titanate nanotube (66.72 mg·g^{-1}), $K_2Ti_6O_{13}/SiO_2$ (14.631 mg·g^{-1}), Fe_3O_4-titanate fiber magnetic composite (37.1 mg·g^{-1}), and other titanate materials, $Na_2La_2Ti_3O_{10}$ has a higher Sr^{2+} adsorption capacity[36–39]. The q_m^{Sr} of $Na_2La_2Ti_3O_{10}$ is also higher than that of traditional adsorption materials such as ZrO_2-Sb_2O_5 (22.21 mg·g^{-1}), thorium tungsten phosphate (57 mg·g^{-1}), Sb(III)/Sb_2O_5 (25.7 mg·g^{-1}), and hex-WO_3 (28 mg·g^{-1})[40–43].

It is important that a material can rapidly capture the target radioactive ions in solutions[44,45]. Thus, the kinetic adsorption experiment was carried out to evaluate the Sr^{2+} capture ability of $Na_2La_2Ti_3O_{10}$ (Fig. 2b). The removal rate R (%) of Sr^{2+} quickly reaches more than 90% within 30 min (Supplementary Tables 5 and 6). The kinetic data of $Na_2La_2Ti_3O_{10}$ for Sr^{2+} capture can be fitted better with the pseudo-second-order kinetics (R^2 = 0.98423) rather than the pseudo-first-order kinetics model (R^2 = 0.93519), which proves that the adsorption process of Sr^{2+} is chemical sorption[46].

The pH values of solutions have a strong influence on the adsorption due to the competition of protons and the influence of the material's acid stability[47]. Therefore, the Sr^{2+} adsorption experiment of $Na_2La_2Ti_3O_{10}$ under a wide pH range has been carried out (Supplementary Fig. 5b and Table 7). In the pH range of 4–12, $Na_2La_2Ti_3O_{10}$ maintains high distribution coefficients ($K_d^{Sr} > 3.68 \times 10^3$ mL·g^{-1}). In particular, it can remove more than 81% of Sr^{2+} ions with the K_d^{Sr} of 4.31×10^3 mL·g^{-1} at pH of 4. Even under strongly alkaline conditions (pH = 12), $Na_2La_2Ti_3O_{10}$ can maintain high removal performance ($K_d^{Sr} = 7.37 \times 10^4$ mL·g^{-1}). However, in the pH range of 1–3, K_d^{Sr} decrease to lower than 103.56 mL·g^{-1}. The significant decrease of K_d^{Sr} is attributed to the competitive adsorption of protons, because H^+ intercalation leads to the formation of the $H_2La_2Ti_3O_{10}$ phase (Supplementary Fig. 3c). The above pH-dependent experiment demonstrates that $Na_2La_2Ti_3O_{10}$ can maintain excellent Sr^{2+} removal capacity in the pH range of 4 to 12.

Sr^{2+} adsorption performances of $Na_2La_2Ti_3O_{10}$ before and after 100 and 200 kGy (kilogray) γ irradiations were studied (Supplementary Table 8). After γ irradiation, the parent structure of $Na_2La_2Ti_3O_{10}$

can remain unchanged, which is confirmed by comparing the PXRD patterns of the pristine and irradiated samples (Supplementary Fig. 5c). The R^{Sr} of the pristine $Na_2La_2Ti_3O_{10}$ is 96.37%, while samples after 100 and 200 kGy γ irradiation can still retain high R^{Sr} (more than 95.12%) (Supplementary Fig. 5d). These results demonstrate that $Na_2La_2Ti_3O_{10}$ has excellent irradiation stability.

Selectivity is one of the important indexes of adsorption materials[48–50]. Therefore, the Sr^{2+} capture performance of $Na_2La_2Ti_3O_{10}$ in the presence of individual Cs^+, K^+, and Ca^{2+} was investigated. When Cs/Sr molar ratios vary from 10.36 to 938.43, the K_d^{Sr} can be maintained in the range from 6.83×10^3 to 1.94×10^4 mL·g^{-1}, corresponding to the R^{Sr} greater than 87%, whereas the K_d^{Cs} are only in the range of 1.28×10^2 to 2.25×10^2 mL·g^{-1} (Fig. 2c and Supplementary Table 9). Even at very high concentration of Cs^+ (Cs/Sr molar ratio up to 4574.04), the K_d^{Sr} of $Na_2La_2Ti_3O_{10}$ still reaches 1.58×10^3 mL·g^{-1}, whereas the K_d^{Cs} is lower than 20 mL·g^{-1}. Similarly, under K/Sr molar ratios of 17.57 to 2633.29, the K_d^{Sr} values of $Na_2La_2Ti_3O_{10}$ can be maintained in the range from 5.3×10^3 to 2.26×10^4 mL·g^{-1}, while the K_d^{K} only vary from 93.50 to 2.44×10^2 mL·g^{-1} (Supplementary Table 10). Apparently, $Na_2La_2Ti_3O_{10}$ can selectively capture Sr^{2+} in the presence of excess Cs^+ and K^+. In addition, K_d^{Sr} range from 5.7×10^3 to 1.86×10^4 mL·g^{-1} ($R^{Sr} > 85\%$) when Ca/Sr molar ratios are in the range of 6.52 to 637.01 (Supplementary Table 11). At the same time, K_d^{Ca} are all lower than 5.13×10^2 mL·g^{-1}. This indicates that in the presence of interfering Ca^{2+} ions, $Na_2La_2Ti_3O_{10}$ can still maintain high Sr^{2+} removal performance.

Further, the selective Sr^{2+} capture ability of $Na_2La_2Ti_3O_{10}$ under the coexistence of K/Ca/Na/Mg/Sr/Cs/Eu/Zr was also investigated. When the mass concentrations of competing ions (K^+, Na^+, Cs^+, Ca^{2+}, and Mg^{2+}) are close to that of Sr^{2+}, the K_d^{Sr} remains higher than 7.24×10^3 mL·g^{-1}, whereas K_d of competing ions (K^+, Na^+, Cs^+, Ca^{2+}, and Mg^{2+}) are all less than 5.56×10^2 mL·g^{-1} (Supplementary Table 12). Even if the mass concentrations of competing ions are five times higher than that of Sr^{2+} under the coexistence of $K^+/Ca^{2+}/Na^+/Mg^{2+}/Sr^{2+}/Cs^+$, the K_d^{Sr} still reaches 3.66×10^3 mL·g^{-1} (Supplementary Table 13). Moreover, the K_d^{Sr} is higher than 2.95×10^4 mL·g^{-1} with the R^{Sr} more than 96.73% when Sr^{2+} coexists with equal mass concentrations of M^{n+} ions (M^{n+} = Cs^+, Eu^{3+}, and Zr^{4+}), while the K_d^{M} are lower than 2.66×10^3 mL·g^{-1} (Supplementary Table 14). Despite the mass concentrations of M^{n+} being five times higher than that of Sr^{2+} under the coexistence of $Sr^{2+}/Cs^+/Eu^{3+}/Zr^{4+}$, the K_d^{Sr} remains above 2.49×10^4 mL·g^{-1} (Supplementary Table 15). Moreover, to evaluate the feasibility of removing Sr^{2+} in actual water systems, the adsorption experiment of $Na_2La_2Ti_3O_{10}$ was further carried out in Sr^{2+}-contaminated actual water samples (Supplementary Table 16). $Na_2La_2Ti_3O_{10}$ shows good removal efficiency of Sr^{2+} in lake water, river water, and tap water with K_d^{Sr} of 3.65×10^3 mL·g^{-1}, 4.24×10^3 mL·g^{-1}, and 6.18×10^3 mL·g^{-1}, respectively.

To study the reusability of $Na_2La_2Ti_3O_{10}$, adsorption-desorption experiments were carried out. The adsorption-desorption efficiency of $Na_2La_2Ti_3O_{10}$ was systematically investigated for four adsorption-desorption cycles. It is found that $Na_2La_2Ti_3O_{10}$ can still maintain the stability of its layered skeleton after four adsorption-desorption cycles, and R^{Sr} can still reach more than 98% (Supplementary Table 17 and Fig. 5e).

$Na_2La_2Ti_3O_{10}$ was also used for the treatment of acidic (pH = 3.75) ^{90}Sr-liquid-waste generated from the production of radioactive sources at CNNC HTA Co., Ltd (Fig. 2d). ^{90}Sr-liquid-waste contains $^{60}Co^{2+}$ and Na^+ ions and so on in addition to $^{90}Sr^{2+}$. The results show that only 5 mg of $Na_2La_2Ti_3O_{10}$ can remove 98.80% of ^{90}Sr from 5 mL acidic ^{90}Sr-liquid-waste, and the ^{90}Sr activity concentration of wastewater is reduced by two orders of magnitude (Supplementary Table 18). When 40 mg of $Na_2La_2Ti_3O_{10}$ is used (solid-liquid ratio $m/V = 8$ mg·mL^{-1}), the R^{Sr} reaches 99.18%. Therefore, a small amount of $Na_2La_2Ti_3O_{10}$ can significantly reduce the radioactivity of acidic radioactive ^{90}Sr wastewater. $Na_2La_2Ti_3O_{10}$ exhibits excellent ^{90}Sr removal performance under actual working conditions, highlighting the current layered titanate-based perovskite as a ^{90}Sr scavenger with practical application potential.

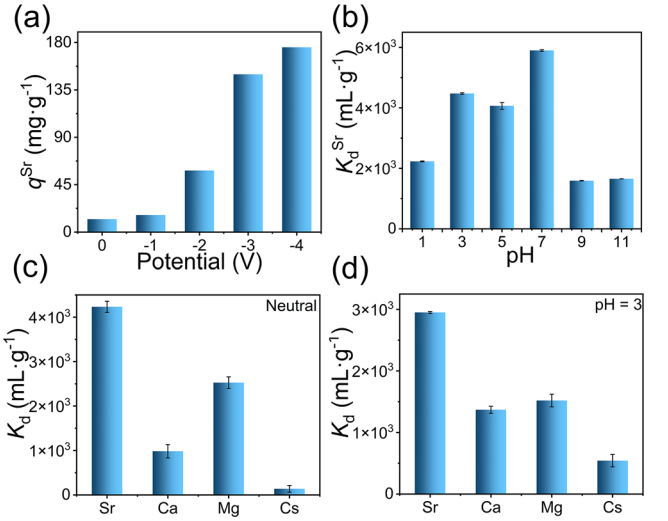

Fig. 3 | The removal performance of C@NaLaTiO for Sr^{2+}. **a** Sr^{2+} adsorption capacity by C@NaLaTiO at different potentials. **b** K_d^{Sr} (mL·g^{-1}) of C@NaLaTiO at various pH values. **c** K_d (mL·g^{-1}) of various metal ions by C@NaLaTiO in the coexistence of K^+, Na^+, Cs^+, Ca^{2+}, Sr^{2+}, and Mg^{2+} under neutral conditions. **d** K_d (mL·g^{-1}) of various metal ions by C@NaLaTiO in the coexistence of K^+, Na^+, Cs^+, Ca^{2+}, Sr^{2+}, and Mg^{2+} at pH of 3. Error bars present the standard deviation of the mean of three experiments. Source data are provided as a Source Data file.

Electrochemical adsorption experiments of C@NaLaTiO

Electrochemical adsorption experiments were carried out in a three-electrode system, in which C@NaLaTiO was the working electrode, carbon cloth was the counter electrode, and the saturated calomel electrode ($Hg/Hg_2Cl_2/KCl$ saturated solution) was the reference electrode. The electrochemical adsorption experiment was performed by applying a potential of 0 to −4 V in 50 mL $SrCl_2{\cdot}6H_2O$ solution ($C_0^{Sr} = 57.89$ mg·L^{-1}) to determine the effect of the voltage on the Sr^{2+} adsorption (Fig. 3a and Supplementary Table 19). In the electrochemically controlled adsorption process, the adsorption capacity remains almost stable in the voltage range of 0 to −1 V. When the negative potential is up from −2 to −4 V, the adsorption capacity begins to increase significantly and finally reaches 175.43 mg·g^{-1}. Compared with the batch adsorption experiment, the adsorption capacity increases from 104.84 mg·g^{-1} to 175.43 mg·g^{-1}. The Sr^{2+} adsorption capacity of C@NaLaTiO is more than that of some Sr^{2+} adsorbents such as FZU-1 (62.84 mg·g^{-1}), SSAC hydrogel (134.40 mg·g^{-1}), and SA-PA-H (151.70 mg·g^{-1})[51–54]. Meanwhile, it is found that the applied voltage has a great influence on the electrochemical adsorption performance; thus, the applied voltage of −4 V was used in the subsequent experiments.

The kinetic study was carried out to evaluate the capture ability of C@NaLaTiO toward Sr^{2+} ions (Supplementary Fig. 6a and Table 20). The concentration of Sr^{2+} decreases rapidly in the neutral aqueous solution as the contact proceeds. After 240 min, the Sr^{2+} adsorption of C@NaLaTiO reaches equilibrium, and the adsorption capacity of Sr^{2+} rapidly achieves 164.29 mg·g^{-1}. Kinetic data of the electrochemical experiment can be well fitted by the pseudo-second-order kinetic model with a high correlation coefficient R^2 of 0.9899 (Supplementary Fig. 6b and Table 21).

In the pH-dependent experiments, C@NaLaTiO shows satisfactory removal rates on Sr^{2+} in a wide pH range. The K_d^{Sr} of C@NaLaTiO reaches 5.90×10^3 mL·g^{-1} at pH of 7 (Fig. 3b and Supplementary Table 22). Importantly, K_d^{Sr} can still be maintained above 10^3 mL·g^{-1} under acidic conditions (pH < 4). Even at pH of 1, C@NaLaTiO can retain efficient adsorption capacity for Sr^{2+} ($K_d^{Sr} = 2.23 \times 10^3$ mL·g^{-1}).

https://doi.org/10.1038/s41467-025-64537-1

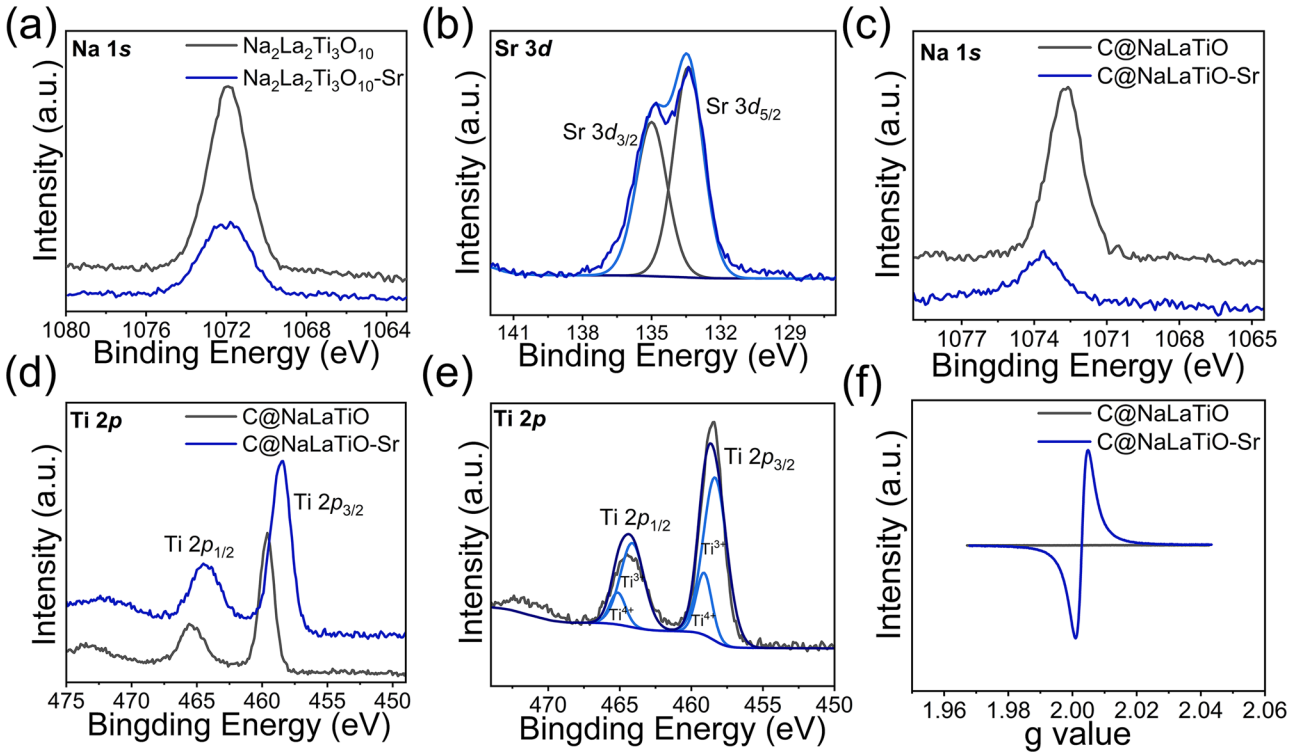

Fig. 4 | The capture mechanism study of $Na_2La_2Ti_3O_{10}$ and C@NaLaTiO for Sr^{2+}. **a** XPS spectra of Na 1*s* for $Na_2La_2Ti_3O_{10}$ and $Na_2La_2Ti_3O_{10}$-Sr. **b** The XPS spectrum of Sr 3*d* for $Na_2La_2Ti_3O_{10}$-Sr. **c** XPS spectra of Na 1*s* for C@NaLaTiO and C@NaLaTiO-Sr. **d** XPS spectra of Ti 2*p* for C@NaLaTiO and C@NaLaTiO-Sr. **e** The XPS spectrum of Ti 2*p* for C@NaLaTiO-Sr. **f** EPR spectra of C@NaLaTiO and C@NaLaTiO-Sr. Source data are provided as a Source Data file.

The Sr^{2+} removal performance of C@NaLaTiO in solutions containing $K^+/Na^+/Cs^+/Sr^{2+}/Ca^{2+}/Mg^{2+}$ was studied. C@NaLaTiO exhibits selective Sr^{2+} capture in complex neutral and acidic solutions with the coexistence of $K^+/Na^+/Cs^+/Sr^{2+}/Ca^{2+}/Mg^{2+}$. Its K_d^{Sr} reaches 4.23×10^3 mL·g^{-1} in neutral solutions, whereas the K_d^M (M^{n+} = K^+, Na^+, Cs^+, Ca^{2+}, and Mg^{2+}) are all lower than 2.53×10^3 mL·g^{-1} (Fig. 3c; K_d^{Na} and K_d^K are shown in Supplementary Tables 23–25). Remarkably, C@NaLaTiO can maintain good Sr^{2+} adsorption capacity under acidic conditions ($K_d^{Sr} = 2.95 \times 10^3$mL·g^{-1} at pH of 3; $K_d^{Sr} = 7.56 \times 10^2$ mL·g^{-1} at pH of 1) (Fig. 3d and Supplementary Fig. 6c, Tables 24 and 25).

To further test the complete electrochemical adsorption and desorption cycle, four cyclic reuse experiments of C@NaLaTiO were carried out. The adsorption process of Sr^{2+} was studied in solutions containing 67.70 mg·L^{-1} Sr^{2+} at −4 V, and the desorption process was carried out in 0.5 mol·L^{-1} NaCl solution at 4 V (Supplementary Fig. 6d and Table 26). The experimental results show that C@NaLaTiO maintains excellent cycling stability and the adsorption capacity remains above 170.32 mg·g^{-1}.

Capture mechanism

X-ray photoelectron spectroscopy (XPS) spectra of $Na_2La_2Ti_3O_{10}$ and $Na_2La_2Ti_3O_{10}$-Sr were tested (Supplementary Fig. 7a and Fig. 4a, b). By comparing the XPS spectra of Na^+, it is found that the characteristic peak of Na 1*s* near 1072 eV is significantly weakened after the adsorption of Sr^{2+} (Fig. 4a)[55]. In XPS of $Na_2La_2Ti_3O_{10}$-Sr, Sr $3d_{5/2}$ and Sr $3d_{3/2}$ characteristic peaks of Sr 3*d* appear at 133.5 eV and 135.1 eV, respectively (Fig. 4b)[55,56]. The above results verify that the Sr^{2+} adsorption of $Na_2La_2Ti_3O_{10}$ is due to the ion exchange between Sr^{2+} and interlayer Na^+ in $Na_2La_2Ti_3O_{10}$.

Moreover, in the above electrochemical adsorption experiments, we found that the adsorption capacity of C@NaLaTiO exceeded the theoretical exchange capacity of $Na_2La_2Ti_3O_{10}$ (139.66 mg·g^{-1}), and the selectivity under acidic conditions was also improved. Therefore, we speculate that in addition to ion exchange, there are redox reactions in C@NaLaTiO that promote the Sr^{2+} adsorption. To verify this point, XPS spectra of C@NaLaTiO and C@NaLaTiO-Sr were tested (Supplementary Fig. 7b). After Sr^{2+} adsorption, the XPS peak intensity of Na 1*s* decreases, indicating that the content of Na^+ reduces (Fig. 4c)[57]. Peaks of Ti $2p_{3/2}$ and Ti $2p_{1/2}$ at 459.6 eV and 465.6 eV can be observed in XPS of C@NaLaTiO, showing the presence of Ti^{4+} (Fig. 4d)[58]. In addition, after the adsorption of Sr^{2+}, the Ti 2*p* peak shifts to the low energy compared with C@NaLaTiO, suggesting that C@NaLaTiO-Sr obtains many electrons, and Ti^{4+} is partially reduced (Fig. 4e)[59]. The distinct Sr $3d_{3/2}$ and Sr $3d_{5/2}$ characteristic peaks in the survey spectrum of C@NaLaTiO-Sr are observed at 135.6 and 133.8 eV, respectively (Supplementary Fig. 7c)[47]. Importantly, compared with $Na_2La_2Ti_3O_{10}$-Sr, the relative intensity of the characteristic peaks of Sr 3*d* in the XPS spectrum of C@NaLaTiO-Sr is stronger, which indicates that C@NaLaTiO has high adsorption capacity for Sr^{2+}.

To investigate the structural evolution during Sr^{2+} adsorption, synchrotron X-ray diffraction (SXRD) patterns of $Na_2La_2Ti_3O_{10}$, $Na_2La_2Ti_3O_{10}$-Sr, and C@NaLaTiO-Sr were collected (Supplementary Fig. 8). Rietveld refinement confirmed the phase purity of the pristine $Na_2La_2Ti_3O_{10}$ (Supplementary Fig. 8a). Upon Sr^{2+} adsorption, both $Na_2La_2Ti_3O_{10}$-Sr and C@NaLaTiO-Sr exhibited peak splitting, particularly in the 004 and 006 reflections (Supplementary Fig. 8b). This splitting may indicate a symmetry lowering, structural distortion, or interlayer displacement induced by Sr^{2+} intercalation. Notably, the relative intensity of the split peaks is higher in C@NaLaTiO-Sr compared with $Na_2La_2Ti_3O_{10}$-Sr, suggesting the higher Sr^{2+} uptake capacity of C@NaLaTiO-Sr.

Since the peak shift of Ti 2*p* is observed in the XPS spectrum of C@NaLaTiO-Sr, the defect structures of C@NaLaTiO and C@NaLaTiO-Sr are further characterized by electron paramagnetic resonance (EPR) (Fig. 4f). Compared with C@NaLaTiO, the EPR spectrum of C@NaLaTiO-Sr shows that the intensity at 2.003 is gradually getting stronger, which is caused by the rise of oxygen vacancy concentration in C@NaLaTiO-Sr[33]. And in the XPS spectrum of C@NaLaTiO-Sr, the Ti

https://doi.org/10.1038/s41467-025-64537-1

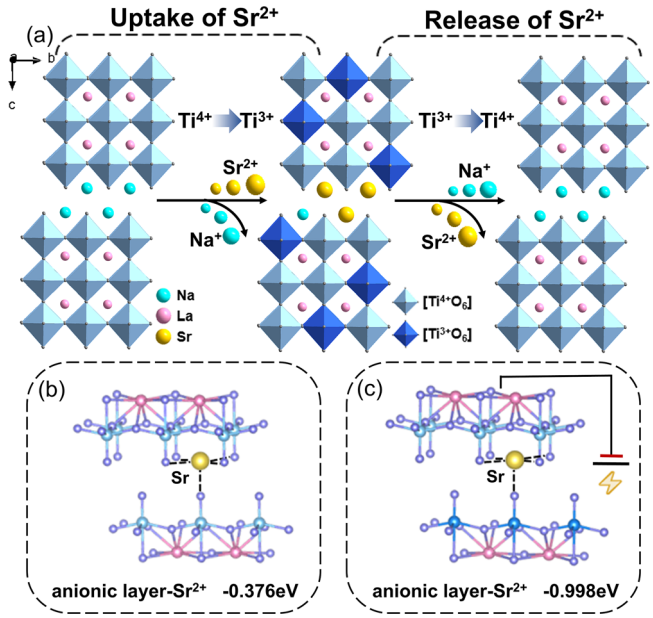

Fig. 5 | Schematic diagram of the "electrochemically switched ion exchange" process and results of density functional theory calculations. a Schematic diagram of the Sr^{2+} adsorption/desorption process of C@NaLaTiO ($[Ti^{4+}O_6]$ octahedra and $[Ti^{3+}O_6]$ octahedra are presented in light blue and dark blue colors, respectively). The calculation on binding energies of the $[La_2Ti_3O_{10}]_n^{2n-}$ layer to Sr^{2+} ions before (**b**) and after applying voltage (**c**).

$2p_{3/2}$ and Ti $2p_{1/2}$ of Ti^{4+} are located at 458.9 eV and 465.1 eV, respectively, and two relatively weak peaks appear at 457.9 eV and 463.5 eV, corresponding to Ti $2p_{3/2}$ and Ti $2p_{1/2}$ of Ti^{3+}, respectively[60]. The reason is the partial reduction of Ti^{4+} to Ti^{3+} under the applied voltage induction, which increases the electron cloud density of oxygen atoms and promotes the formation of oxygen vacancies. When Ti^{3+} is transformed to Ti^{4+} after applying the opposite voltage, two Ti $2p$ peaks in C@NaLaTiO-Sr XPS appear at 459.4 eV (Ti $2p_{3/2}$) and 465.2 eV (Ti $2p_{1/2}$), respectively, and the oxygen electron cloud density decreases (Supplementary Fig. 7d). Consequently, Sr^{2+} is successfully released (Supplementary Fig. 7e). Thus, the electrochemical adsorption and desorption of Sr^{2+} is achieved. Therefore, the XPS, SXRD, and EPR confirm that the capture mechanism of C@NaLaTiO for Sr^{2+} is the ion exchange between Sr^{2+} and interlayer Na^+ in $Na_2La_2Ti_3O_{10}$ and electrochemical reduction of Ti^{4+} to Ti^{3+} under −4 V potential, which generates oxygen vacancies and promotes Sr^{2+} adsorption. Conversely, when the negative voltage (4 V) is applied to the electrode, the reverse oxidation of Ti^{3+} to Ti^{4+} reduces the oxygen vacancies and facilitates the desorption of Sr^{2+} (Fig. 5a).

Density functional theory calculations

In order to further elucidate the mechanism of introducing ESIX to increase the adsorption capacity of Sr^{2+}, density functional theory (DFT) calculations on the interaction of the $[La_2Ti_3O_{10}]_n^{2n-}$ layer with Sr^{2+} ion before and after applying the voltage (−4 V) were performed. The DFT results reveal that the binding energy of the anionic $[La_2Ti_3O_{10}]_n^{2n-}$ layer to Sr^{2+} decreases from −0.376 eV to −0.998 eV under the action of the electric field (Fig. 5b, c). The binding energy of Sr^{2+} to the anionic layer $[La_2Ti_3O_{10}]_n^{2n-}$ during electrochemical adsorption is more negative than that of batch adsorption, suggesting a stronger interaction between the anionic layer $[La_2Ti_3O_{10}]_n^{2n-}$ and the Sr^{2+} ions under the influence of the applied voltage. And it is easier to replace Na^+ ions with Sr^{2+} ions in the interlayer when the voltage is applied. DFT results indicate that through using the method of ESIX, as the voltage is applied, $Na_2La_2Ti_3O_{10}$ shows a much higher adsorption capacity for Sr^{2+} from the energy perspective, providing a more efficient way to remove specific ions from solutions.

Discussion

We develop an efficient strategy for Sr^{2+} capture through an environmentally friendly ESIX method using an electroactive titanate-based perovskite ($Na_2La_2Ti(IV)_3O_{10}$) with exceptional acid and irradiation resistance, and thermal stability. It demonstrates an excellent treatment capability for actual acidic ^{90}Sr-liquid-waste generated during industrial production. Comprehensive characterizations (SXRD, EDS, XPS, EPR) reveal that Sr^{2+} capture and release occur through Na^+/Sr^{2+} ion exchange and electrochemically controlled Ti^{3+}/Ti^{4+} redox reactions, enabling efficient electrochemical adsorption and desorption. DFT calculations further confirm that the introduction of ESIX significantly enhances the Sr^{2+} adsorption capacity of $Na_2La_2Ti_3O_{10}$. By synergistically combining ion exchange with electrochemical adsorption, the current strategy provides a sustainable approach to Sr^{2+} removal and lays the foundation for the development of more efficient materials for radiostrontium treatment. Ultimately, this work expands the potential of electroactive titanate-based perovskites for Sr^{2+} capture via ESIX, supporting the safe and sustainable advancement of the nuclear industry.

Methods

Materials

Na_2CO_3 (AR, Shanghai Hongguang Chemical Plant Co., Ltd), TiO_2 (RG, Acros), La_2O_3 (99.99%, Sinopharm Chemical Reagent Co., Ltd), HNO_3 (65-68%, Sinopharm Chemical Reagent Co., Ltd), NaOH (AR, Tianjin Guangfu Reagent Co., Ltd), CsCl (99.99%, Shanghai Longjin Metallic Material Co., Ltd), KCl (AR, Tianjin Fuchen Chemical Reagent Co., Ltd), NaCl (AR, Sinopharm Chemical Reagent Co., Ltd), $CaCl_2{\cdot}2H_2O$ (74%, Shanghai Sili Chemical Plant), $MgCl_2$ (AR, Adamas Reagent Co., Ltd), $SrCl_2{\cdot}6H_2O$ (AR, Tianjin Guangfu Reagent Co., Ltd), $EuCl_3{\cdot}6H_2O$ (AR, RUIKE State Engineering Research Center of Rare Earth Metallurgy and Functional Materials Co., Ltd), $ZrOCl_2{\cdot}8H_2O$ (98%, Adamas Reagent Co., Ltd), carbon black (CP, Qingdao Chenyang Graphite Co., Ltd), polyvinylidene fluoride (PVDF) (99%, Shanghai McLean Biochemical Technology Co., Ltd), N-methylpyrrolidone (NMP) (AR, Sinopharm Chemical Reagent Co., Ltd), carbon cloth (Suzhou Zhengtairong New Material Co., Ltd). All the chemicals were used without further purification. For economic and safety reasons, we used non-radioactive strontium instead of radionuclide strontium in the batch adsorption and electrochemical adsorption experiments. Radionuclide strontium was only used in the actual treatment of acidic ^{90}Sr-liquid-waste generated from the production of radioactive sources at CNNC HTA Co., Ltd.

Synthesis of $Na_2La_2Ti_3O_{10}$ and C@NaLaTiO

According to the previously reported synthesis method, $Na_2La_2Ti_3O_{10}$ was prepared by the solid phase reaction[34]. Na_2CO_3 (2.8 mmol, 0.2968 g), TiO_2 (6 mmol, 0.4792 g), and La_2O_3 (2 mmol, 0.6516 g) were mixed stoichiometrically and ground well. The mixture was placed in a 20 mL round-bottomed alumina crucible and kept at 900 °C for 24 h, followed by cooling slowly for 48 h to RT. Products were rinsed several times with deionized water and ethanol, and they were separated by filtration and finally dried in an oven at 80 °C overnight to obtain white powder $Na_2La_2Ti_3O_{10}$ as pure phase. About 1.1936 g of $Na_2La_2Ti_3O_{10}$ could be obtained with a yield of 95.12% (based on Ti), which is stable in water and air. The synthesized $Na_2La_2Ti_3O_{10}$, carbon black, and PVDF were dispersed into NMP at a mass ratio of 8:1:1 at RT and dried in an oven at 60 °C overnight. The prepared slurry was coated on the carbon cloth (1.0 × 1.0 cm^2) as the working electrode (C@NaLaTiO).

Characterizations

PXRD patterns were obtained at RT using a Miniflex II diffractometer with Cu$K\alpha$ (λ = 1.54178 Å) at 30 kV and 15 mA within the angular range

of $2\theta = 5–65°$. Elemental analysis and mapping of the samples were performed using a JEOL JSM-6700F SEM and energy-dispersive X-ray spectroscopy (EDS). Solid-state optical diffuse reflectance spectra were recorded on a Shimadzu 2600 UV/vis spectrometer at RT in the range of 800–200 nm. TGA was performed on a NETZSCH STA 449F3 DTA-TG analyzer under a N_2 atmosphere from RT to 1200 °C with a ramp rate of 10 °C·min^{-1}. XPS was performed on the ThermoFisher ESCALAB 250Xi XPS spectrometer system, with all binding energies referenced to the C1*s* peak of adventitious carbon at 284.8 eV. EPR was recorded using an EPR spectrometer (Elexsys E500, Bruker, Germany). Metal ion concentrations in solutions were determined by inductively coupled plasma mass spectrometry (ICP-MS) or inductively coupled plasma optical emission spectrometry (ICP-OES), utilizing an XSeries II and a Thermo 7400 instrument, respectively. Powder SXRD data were collected at SPring-8's BL02B2 beamline (Japan) using high-energy radiation ($\lambda = 0.42$ Å). The samples were encapsulated in borosilicate capillaries before measurement. Structural refinement was subsequently performed using GSAS software. The pH of all solutions was measured with Shanghai Lexmark Electronics 201F. The supernatant was separated using the G16-WS centrifuge. Electrochemical tests were conducted using an electrochemical workstation (CHI660E, CH Instruments, China). Samples were irradiated with *γ*-rays at a total dose of 100 kGy (1.2 kGy·h^{-1} for 89 h) and 200 kGy (1.2 kGy·h^{-1} for 175 h) using a ^{60}Co irradiation source (2 million curies) provided by the Detection Center of Suzhou CNNC Huadong Radiation Co., Ltd, China.

Density functional theory calculations

All the calculations are performed in the framework of the DFT with the projector augmented plane-wave method, as implemented in the Vienna ab initio simulation package (VASP, version number 5.4.4)[61]. The generalized gradient approximation proposed by Perdew, Burke, and Ernzerhof is selected for the exchange-correlation potential[62]. The long-range van der Waals interaction is described by the DFT-D3 approach[63]. The cut-off energy for the plane wave is set to 500 eV. The energy criterion is set to 10^{-6} eV in the iterative solution of the Kohn–Sham equation. The K-mesh resolved in real space is 0.04 2π·Å^{-1}. All the structures are relaxed until the residual forces on the atoms have declined to less than 0.02 eV·Å^{-1}.

Data availability

The ion exchange data generated in this study are provided in the Supplementary Information/Source Data file. Source data are provided in this paper. Additional information can be obtained from the corresponding author upon request. Source data are provided with this paper.

References

1. Zhang, F. L., Wang, J. L., Bi, Q. Q. & Du, J. Z. ^{90}Sr in seawater of the East China Sea: Inventory, new potential source, and environmental implications. *Sci. Total Environ.* **764**, 144266 (2021).
2. Inan, S. Inorganic ion exchangers for strontium removal from radioactive waste: a review. *J. Radioanal. Nucl. Chem.* **331**, 1137–1154 (2022).
3. Tang, J. H., Sun, H. Y., Ma, W., Feng, M. L. & Huang, X. Y. Recent progress in developing crystalline ion exchange materials for the removal of radioactive ions. *Chin. J. Struct. Chem.* **39**, 2157–2171 (2020).
4. Zhang, J. R. et al. Distinctive two-step intercalation of Sr^{2+} into a coordination polymer with record high ^{90}Sr uptake capabilities. *Chem* **5**, 977–994 (2019).
5. Wang, K. T. et al. One-pot preparation of NaA Zeolite microspheres for highly selective and continuous removal of Sr(II) from aqueous solution. *ACS Sustain. Chem. Eng.* **7**, 2459–2470 (2019).
6. Casacuberta, N., Masqué, P., Garcia-Orellana, J., Garcia-Tenorio, R. & Buesseler, K. O. ^{90}Sr and ^{89}Sr in seawater off Japan as a consequence of the Fukushima Dai-ichi nuclear accident. *Biogeosciences* **10**, 3649–3659 (2013).
7. Rahman, R. O. A., Ibrahium, H. A. & Hung, Y. T. Liquid radioactive wastes treatment: a review. *Water* **3**, 551–565 (2011).
8. Ding, D. H., Zhang, Z. Y., Lei, Z. F., Yang, Y. N. & Cai, T. M. Remediation of radiocesium-contaminated liquid waste, soil, and ash: a mini review since the Fukushima Daiichi Nuclear Power Plant accident. *Environ. Sci. Pollut. Res.* **23**, 2249–2263 (2016).
9. Bian, Y. Y. et al. Highly selective separation of Cs^+ from brines using an electroactive layered composite of vanadosilicate. *ACS Sustain. Chem. Eng.* **11**, 10884–10894 (2023).
10. Wang, B. Y. et al. Electrochemical adsorption of cesium using a nickel hexacyanoferrate-doped porous carbon electrode. *J. Radioanal. Nucl. Chem.* **332**, 2589–2600 (2023).
11. Liao, S. L. et al. Simultaneous separation of iodide and cesium ions from dilute wastewater based on PPy/PTCF and NiHCF/PTCF electrodes using electrochemically switched ion exchange method. *Sep Purif. Technol.* **139**, 63–69 (2015).
12. Su, J. Y. et al. The characterization and application of prussian blue at graphene coated carbon fibers in a separated adsorption and electrically switched ion exchange desorption processes of cesium. *Electrochim. Acta* **230**, 399–406 (2017).
13. Sun, B. et al. Separation of low concentration of cesium ion from wastewater by electrochemically switched ion exchange method: Experimental adsorption kinetics analysis. *J. Hazard Mater.* **233**, 177–183 (2012).
14. Bian, Y. Y. et al. Highly selective capture of cesium using an electrochemically renewable molybdenum-based crystalline adsorbent. *J. Environ. Chem. Eng.* **12**, 111931 (2024).
15. Liu, X. J., Wu, J. L. & Wang, J. L. Electro-adsorption of Sr(II) from aqueous solution by activated carbon cloth/nickel hexacyanoferrate composite electrode through capacitive deionization. *J. Clean. Prod.* **380**, 135075 (2022).
16. Choi, H., Do, K., Park, S., Yu, J. S. & Ko, J. Efficient hole transporting materials with two or four *N*, *N*-Di(4-methoxyphenyl)aminophenyl arms on an ethene unit for perovskite solar cells. *Chem. Eur. J.* **21**, 15919–15923 (2015).
17. Huang, L. et al. Research progresses on the application of perovskite in adsorption and photocatalytic removal of water pollutants. *J. Hazard Mater.* **442**, 130024 (2023).
18. Wang, W., Tadé, M. O. & Shao, Z. P. Research progress of perovskite materials in photocatalysis- and photovoltaics-related energy conversion and environmental treatment. *Chem. Soc. Rev.* **44**, 5371–5408 (2015).
19. Hsu, Y. C., Chang, S. H., Chung, W. C. & Chang, M. B. Photocatalytic removal of trichloroethylene from water with $LaFeO_3$. *Environ. Sci. Pollut. Res.* **26**, 26276–26285 (2019).
20. Zhang, J. B. et al. Nitrogen-doped perovskite as a bifunctional cathode catalyst for rechargeable lithium oxygen batteries. *ACS Appl. Mater. Interfaces* **10**, 5543–5550 (2018).
21. Hu, Y. Z. et al. Superior sorption capacities of Ca-Ti and Ca-Al bimetallic oxides for U(VI) from aqueous solutions. *Chem. Eng. J.* **316**, 419–428 (2017).
22. Lu, S. H. et al. Influence of carbonate on sequestration of U(VI) on perovskite. *J. Hazard Mater.* **364**, 100–107 (2019).
23. Chitrakar, R. et al. $HCa_2Nb_3O_{10}$•$1.5H_2O$ as an ion exchanger for NH_4^+ ion removal. *Ind. Eng. Chem. Res.* **47**, 176–179 (2008).
24. Li, X. T., Hoffman, J. M. & Kanatzidis, M. G. The 2D halide perovskite rulebook: How the spacer influences everything from the structure to optoelectronic device efficiency. *Chem. Rev.* **121**, 2230–2291 (2021).
25. Chitrakar, R., Makita, Y. & Sonoda, A. Cesium ion decontamination by layered perovskite $HCa_2Nb_3O_{10}$ center dot $1.5H_2O$. *Bull. Chem. Soc. Jpn* **86**, 1419–1425 (2013).

26. Sun, H. Y. et al. Boosting selective Cs^+ uptake through the modulation of stacking modes in layered niobate-based perovskites. *Nat. Commun.* **15**, 8681 (2024).
27. Gopalakrishnan, J. & Bhat, V. $A_2Ln_2Ti_3O_{10}$ (*A* = potassium or rubidium; Ln = lanthanum or rare earth): a new series of layered perovskites exhibiting ion exchange. *Inorg. Chem.* **26**, 4299–4301 (1987).
28. Nozaki, R. et al. Vibrational study of layered perovskites $M_2La_2Ti_3O_{10}$ (*M* = Li, Na, K, Rb): Raman spectra and normal mode analysis. *J. Phys. Chem. B* **105**, 7950–7953 (2001).
29. Toda, K., Kameo, Y., Kurita, S. & Sato, M. Crystal structure determination and ionic conductivity of layered perovskite compounds $NaLnTiO_4$ (Ln=rare earth). *J. Alloy. Compd.* **234**, 19–25 (1996).
30. Kawashima, K. et al. Understanding the effect of partial N^{3-}-to-O^{2-} substitution and H^+-to-K^+ exchange on photocatalytic water reduction activity of Ruddlesden-Popper layered perovskite $KLaTiO_4$. *Mol. Catal.* **432**, 250–258 (2017).
31. Li, M. C. et al. Enhanced adsorption of cesium ions by electrochemically switched ion exchange method: based on surface-synthetic $Na_2Ti_3O_7$ nanotubes. *Colloids Surf. A* **579**, 123712 (2019).
32. McCafferty, E. & Wightman, J. P. Determination of the concentration of surface hydroxyl groups on metal oxide films by a quantitative XPS method. *Surf. Interface Anal.* **26**, 549–564 (1998).
33. Meng, W. J., Dang, Z. Z., Li, D. S. & Jiang, L. Long-cycle-life sodium-ion battery fabrication via a unique chemical bonding interface mechanism. *Adv. Mater.* **35**, 2301376 (2023).
34. Toda, K., Kameo, Y., Fujimoto, M. & Sato, M. Crystal-structure and ionic-conductivity of a layered perovskite, $Na_2La_2Ti_3O_{10}$. *J. Ceram. Soc. Jpn* **102**, 737–741 (1994).
35. Duong D. D. *Adsorption Analysis: Equilibria and Kinetics* (Journal of the Ceramic Society of Japan, 1998).
36. Chen, Z. et al. Selective removal of Sr^{2+} by cation exchange using silica-based titanate adsorbents. *J. Solid State Chem.* **312**, 123247 (2022).
37. Li, C. M. et al. Studies on the separation and in-situ sintering solidification of strontium by a highly-efficient titanate-based adsorbent. *Microporous Mesoporous Mater.* **288**, 109607 (2019).
38. Kasap, S., Piskin, S. & Tel, H. Titanate nanotubes: preparation, characterization and application in adsorption of strontium ion from aqueous solution. *Radiochim. Acta* **100**, 925–929 (2012).
39. Yi, R., Ye, G. & Chen, J. Synthesis of core-shell magnetic titanate nanofibers composite for the efficient removal of Sr^{2+}. *RSC Adv.* **9**, 27242–27249 (2019).
40. Igarashi, S., Sato, S., Takashima, T. & Ogawa, M. Preparation of finite particles of layered niobate ($KCa_2Nb_3O_{10}$) for improved materials performance. *Ind. Eng. Chem. Res.* **52**, 3329–3333 (2013).
41. Yavari, R., Khanchi, A. R., Maragheh, M. G. & Waqif-Husain, S. Sorption of radionuclides on thorium tungstophosphate: a new inorganic ion-exchanger. *J. Radioanal. Nucl. Chem.* **267**, 685–690 (2006).
42. Zhang, L. et al. Strontium(II) adsorption on Sb(III)/Sb_2O_5. *Chem. Eng. J.* **267**, 245–252 (2015).
43. Li, X. L. et al. Adsorption kinetic, isotherm and thermodynamic studies of Sr^{2+} onto hexagonal tungsten oxide. *J. Radioanal. Nucl. Chem.* **298**, 47–53 (2013).
44. Tai, B. et al. Flexible interdigitated layered framework with multiple accessible active sites for high-performance CH_3I capture. *Sci. China Chem.* **67**, 1569–1577 (2024).
45. Xie, Y. H. et al. Recent progress of radionuclides separation by porous materials. *Sci. China Chem.* **67**, 3515–3577 (2024).
46. Ho, Y. S. Review of second-order models for adsorption systems. *J. Hazard Mater.* **136**, 681–689 (2006).
47. Guo, Y. L. et al. Efficient removal of Sr^{2+} ions by a one-dimensional potassium phosphatoantimonate. *Chem. Eng. J.* **460**, 141697 (2023).
48. Lv, C. et al. Efficient uranium adsorption of low-cost and eco-friendly MQ_2-collagen fibers (*M* = Mo, W; *Q* = S, Se) composite materials prepared by co-ball milling. *Natl Sci. Open* **4**, 20240029 (2024).
49. Tang, J. H., Feng, M. L.& Huang, X. Y. Metal chalcogenides as ion-exchange materials for the efficient removal of key radionuclides: a review. *Fundam. Res.* https://doi.org/10.1016/j.fmre.2023.1010.1022 (2023).
50. Zhang, X. et al. Emerging MOFs, COFs, and their derivatives for energy and environmental applications. *Innovation* **6**, 100778 (2025).
51. Zheng, B. T. et al. Inverse vulcanization-induced self-assembly of polysulfide into responsive micelles and their templated hydrogel adsorbent for Sr^{2+} removal. *Langmuir* **41**, 11614–11629 (2025).
52. Liu, Y. X. et al. Site differentiation strategy for selective strontium uptake and elution within an all-inorganic polyoxoniobate framework. *Nat. Commun.* **15**, 8896 (2024).
53. Li, L. et al. A negatively-charged supramolecular trap for precisely catching strontium ion. *Nat. Commun.* **16**, 2606 (2025).
54. Zheng, B. T. et al. Thiol-rich and ion-imprinted alginate hydrogel as a highly adsorptive and recyclable filtration membrane for rapid and selective Sr(II) removal. *Chem. Eng. J.* **465**, 142752 (2023).
55. Moulder, J. F., Chastain, J. & King, R. C. Handbook of X-ray photoelectron spectroscopy: a reference book of standard spectra for identification and interpretation of XPS data. *Chem. Phys. Lett.* **220**, 7–10 (1992).
56. Yuan, Z. et al. Synthesis and properties of Sr^{2+} doping alpha-tricalcium phosphate at low temperature. *J. Appl Biomater. Funct. Mater.* **19**, 1–8 (2021).
57. Zhao, Z. W. et al. XPS and FTIR studies of sodium arsenate vitrification by cullet. *J. Non-Cryst. Solids* **502**, 254–254 (2018).
58. Ouyang, J. L., Sun, X. T., Chen, X. S., Chen, J. Y. & Zhuang, X. M. Preparation of layered bioceramic hydroxyapatite/sodium titanate coatings on titanium substrates using a hybrid technique of alkali-heat treatment and electrochemical deposition. *J. Mater.* **49**, 1882–1892 (2014).
59. Ni, J. F. et al. Superior sodium storage in $Na_2Ti_3O_7$ nanotube arrays through surface engineering. *Adv. Energy Mater.* **6**, 1502568 (2016).
60. Fu, S. D., Ni, J. F., Xu, Y., Zhang, Q. & Li, L. Hydrogenation driven conductive $Na_2Ti_3O_7$ nanoarrays as robust binder-free anodes for sodium-ion batteries. *Nano Lett.* **16**, 4544–4551 (2016).
61. Kresse, G. & Joubert, D. From ultrasoft pseudopotentials to the projector augmented-wave method. *Phys. Rev. B* **59**, 1758–1775 (1999).
62. Perdew, J. P., Burke, K. & Ernzerhof, M. Generalized gradient approximation made simple. *Phys. Rev. Lett.* **77**, 3865–3868 (1996).
63. Grimme, S., Antony, J., Ehrlich, S. & Krieg, H. A consistent and accurate ab initio parametrization of density functional dispersion correction (DFT-D) for the 94 elements H-Pu. *J. Chem. Phys.* **132**, 154104 (2010).

Acknowledgements

We greatly thank the financial support from the National Natural Science Foundation of China, the Natural Science Foundation of Fujian Province, and the Strategic Priority Research Program of the Chinese Academy of Sciences. M.F. was supported by the National Natural Science Foundation of China (Nos. 22325605 and U21A20296) and the Strategic Priority Research Program of the Chinese Academy of Sciences (No. XDB1170000). Z.L. was supported by the Major Program of the National Natural Science Foundation of China (Nos. 22494680 and 22494684) and the Key Program of the National Natural Science Foundation of China (No. 22336006). H.S. was supported by the National Natural Science Foundation of China (No. 22406185) and the Natural Science Foundation of Fujian Province (No. 2024J08105).

Author contributions

The manuscript was written through the contributions of all authors. Z.C., X.H., M.F., and Z.L. conceived the project. Z.C. designed and performed most of the experiments and analyzed the data. F.D., S.J., H.S., S.L., and J.T. offered help in the partial experiments. Z.C. prepared the manuscript. M.F., Z.L., F.D., and X.H. revised the manuscript. M.F. and Z.L. supervised the project.

Competing interests

The authors declare no competing interests.

Additional information

Supplementary information The online version contains supplementary material available at https://doi.org/10.1038/s41467-025-64537-1.

Correspondence and requests for materials should be addressed to Mei-Ling Feng or Zhang Lin.

Peer review information *Nature Communications* thanks Yubing Sun, and the other, anonymous, reviewer(s) for their contribution to the peer review of this work. A peer review file is available.